Performance evaluation of combined solar chimney and radiative cooling ventilation

Suhendri Suhendri[1], Mingke Hu[1,*], Yuehong Su[1,*], Jo Darkwa[1], Saffa Riffat[1]

[1] Department of Architecture and Built Environment, University of Nottingham, *Nottingham NG7 2RD, UK*

*Corresponding author: mingke.hu@nottingham.ac.uk; yuehong.su@nottingham.ac.uk

Abstract:

Passive cooling is inevitable for buildings to be resilient to global warming. While many forms of passive cooling techniques have been developed, passive radiative cooling (RC), as an emerging technology, is still not widely applied in buildings. Due to current limitations, many proposals for implementing RC in buildings have come up in combination with other passive design strategies. In this study, we propose to combine RC with natural ventilation in the form of a novel RC-enhanced roof solar chimney (SC-RC) ventilation and present an evaluation of its ventilation and thermal performance. A hypothetical room equipped with SC on the sun-facing side of the roof, and RC cavity on the opposite side, was developed. Three different opening configurations were arranged as the case studies, namely 'SC+wall-opening', 'SC-RC', and 'SC-RC+wall-opening'. Computational fluid dynamics (CFD) using ANSYS Fluent 2021 was employed to simulate the case studies. The results indicate that the RC cavity improves the ventilation and cooling performance of the natural ventilation system. In terms of ventilation performance, the 'SC-RC+wall-opening' case is observed to be superior to the conventional 'SC+wall-opening' case, with a daily average ventilation rate of 1.2 ACH daily (required minimum: 0.7 ACH). Likewise, the cooling performance of 'SC-RC' and 'SC-RC+wall-opening' cases are also better than the case without RC cavity.

Keywords: passive cooling, natural ventilation, radiative cooling, solar chimney

Nomenclature		Abbreviations	
F	inclination angle factor	ACH	air change per hour
g	gravitational acceleration (9.81 m·s^{-2})	CFD	computational fluid dynamics
H	solar irradiance (W·m^{-2})	PCM	phase change material

h	heat transfer coefficient ($W \cdot m^{-2} \cdot K^{-1}$)	PE	polyethylene
P	static (gauge) pressure (Pa)	PT	photothermal
q	heat flux ($W \cdot m^{-2}$)	PV	photovoltaics
T	temperature (°C)	RC	radiative cooling
U	thermal transmittance ($W \cdot m^{-2} \cdot K^{-1}$)	RMSD	root mean square deviation
v	wind speed ($m \cdot s^{-1}$)	SC	solar chimney
z	vertical distance (m)	SH	solar heater
		TMY	typical meteorological year
Greek letters		UDF	user-defined function
α	thermal expansion coefficient of air		
ΔP	pressure difference (Pa)	Subscript	
ΔT	temperature difference (°C)	abs	absorber
ε	emissivity	amb	ambient
ρ	density ($kg \cdot m^{-3}$)	rad	radiation
σ	Stefan-Boltzmann constant (5.67×10^{-8} $W \cdot m^{-2} \cdot K^{-4}$)	sol	solar
		surf	building's surface
τ	transmissivity		

1. Introduction

Global warming demands buildings to be more frequently cooled to the comfort range, as indicated by the skyrocket of the air-conditioning (AC) selling in the last three decades [1]. Yet, this very cooling demand, if supplied by greenhouse-gases-emitting processes, contributes to an even warmer earth. Thus, to break this cycle of cause and effect, the cooling demands of buildings should be supplied from a renewable resource or using a passive cooling technique.

In the field of passive cooling for buildings, radiative cooling (RC) is considered novice compared to convective and evaporative cooling technologies. As its name suggests, RC is a cooling mechanism that happens due to heat transfer via radiation from the earth's surface to the sky. As the sky effective temperature is generally lower than any terrestrial body and the fact that the atmosphere is transparent to long-wave radiation of 8-13 μm wavelength, these two conditions make the RC possible [2,3]. This phenomenon has long been used traditionally for ice-making in some old civilisations [4]. As for application in building, it was once utilised for nocturnal cooling in

the mid-20th century. Only recently, research for the application of RC in buildings was revived due to the development in material technologies [5–7]. A typical RC panel places an RC emitter inside a fully insulated frame and protects it from convective heat loss by a cover that is transparent, especially in the atmospheric band (8-13 μm). A polyethylene (PE) film is commonly used as the cover, and this makes the conventional RC emitter not durable. Thus, a durable cover shield for the RC itself is now one of the pursued topics in the RC research [8–10].

The current state-of-the-art of building-integrated radiative cooling (BIRC) manifests into two broad ways of implementation, i.e., active systems or passive systems. The BIRC with the active system works with the assistance of any mechanical device(s), whereas the passive system operates fully passively. Active BIRC systems are commonly combined with air-conditioning devices (AC) [11–14]. In its combination with AC, the BIRC emitter is used to provide chilled water for the cooling coil of AC, enabling the system to be more energy-efficient [11–13].

Furthermore, the passive BIRC can be formed as an independent RC emitter, but most often, it is proposed in combination with a phase change material (PCM) [15–17], thermal mass [18,19], or Trombe wall [20]. In quite similar systems proposed by He et al. [15] and Shen et al. [16], an RC module is mounted on the outer side of the wall, incorporated with PCM on the inner side of the wall to store the cooling energy. The cooling energy is transferred from the RC emitter to the PCM by a heat pipe utilising the thermosyphon phenomenon. Different from the RC-PCM system that stores the cooling energy in a PCM, Etzion and Erell [19] used thermal mass in a roof-mounted RC-thermal mass design. BIRC had also been proposed to enhance the performance of a Trombe wall. One example from Sameti and Kasaeian [20] attempted to exploit the RC effect from the inner side of the Trombe wall during the night in the cooling season. The concept is rather like the dual-functional solar heating (SH)-RC module, that is to collect heat during the day and radiate heat during the night, thus optimising the idle time of any conventional stand-alone SH or RC module.

Although many prototypes for BIRC have been developed, researchers are still faced with some challenges for the real application for BIRC, such as the low cooling power of RC, durability of the cover materials, and the maintenance issue [21]. The emitter's performance is also highly constraint by climatic factors such as sky condition, wind speed, atmospheric particles, and air humidity [7,22]. However, two valuable lessons can be derived to overcome the challenges from the precedent of active and passive BIRC systems mentioned previously. Firstly, BIRC is applied in combination with other already established cooling techniques. Secondly, RC can be

used to extend the working time of a system that only works during the daytime, such as SH or PV. So, what was thought of as an idle time for SH/PV at night can be employed as the working time for RC. It is important to note that, although combinations of RC with an active/mechanical cooling technique are not uncommon, concepts for a fully passive application of RC have arguably more advantage in reducing energy used in buildings.

One possible way to apply RC fully passively in buildings is by combining it with a natural ventilation strategy. Among natural ventilation strategies, solar chimney (SC) has the potential to be improved by RC. Solar chimneys can be utilised in two different building elements, on the roof or in the wall. Roof solar chimney is integrated with inclined roof [23–26], or inclined solar chimney on a flat roof [27–30]. Whereas, solar chimney in the wall usually is designed as a façade element [31–34].

As a widely adopted natural ventilation strategy, SC ventilation is still open for improvement, such as extending its working time in the absence of solar radiation, improving its ventilation rate, and enhancing its cooling performance. To extend the working time of SC to the night and make it more stable in the cloudy time, researchers commonly incorporated a PCM material to the SC absorber [35–37]. For ventilation and cooling performance improvements, various strategies have been proposed, and many of them are by combining SC with other natural ventilation or passive cooling techniques. Trombe wall [38], wind catcher [39], an earth-to-air heat exchanger (EAHX) [40–42], water spray [43,44], and cooling cavity [45–47] are some examples of natural ventilation and passive cooling techniques recently combined with SC. In all combinations of SC with passive cooling techniques, the cooling techniques act as a passive precooling system for the inlet air [38,42]. Reviewing the three aspects of improvement for SC ventilation mentioned earlier and some combination strategies that had been developed, we view that RC could be a potential enhancement strategy for SC.

In this research, we proposed and examined a combination of RC with SC in the form of a novel roof solar chimney-radiative cooling (SC-RC) ventilation. The schematic of the proposed SC-RC ventilation is shown in Figure 1. The SC is placed on the sun-facing side of the roof, combined with an RC cavity on the opposite side. During the daytime, the SC is heated by solar radiation to generate a buoyancy effect to draw air from the room and the RC cavity. While the air flows through the RC cavity, it gets cooled by the RC surface and provides chilled air for the room. At night, sky radiative cooling at the RC cavity causes a negative buoyancy to induce a downward airflow for ventilation. It is also worth mentioning that the roof SC-RC ventilation implemented in this strategy has a notable difference from the conventional RC emitter, i.e., we eliminate the convection cover. This elimination of convection cover aims to avoid the use of short-lived material and thus make this SC-RC system

more durable because most of the RC emitter materials are more durable than the commonly used cover material such as polyethylene (PE) [48–50].

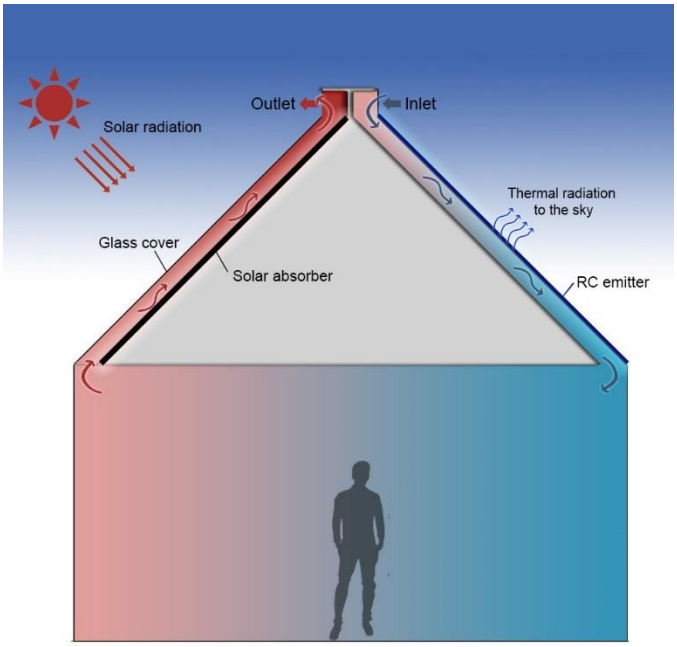

Figure 1 Schematic diagram of roof solar chimney combined with radiative cooling cavity

Furthermore, because in this study we deal with natural ventilation, we used the computational fluid dynamics (CFD) method using ANSYS Fluent 2021 to simulate our case. In the field of RC research, usually, the numerical methods developed by researchers have focused mainly on the modelling of radiation heat transfer, especially for the non-grey model, which is at the heart of RC phenomena. To our best knowledge, this study is the first to model the RC and natural ventilation phenomena using ANSYS Fluent. The CFD code may be well-established for modelling natural ventilation, but the RC simulation needs to be taken thoughtfully, especially because it is combined with a buoyancy-driven flow simulation. Thus, this research also reports the reliability of ANSYS Fluent for the use of RC research.

2. Description of the Case Studies

2.1. Case studies

To evaluate the performance of the SC-RC ventilation, we devised a hypothetical building located in a Mediterranean climate of Athens (37.9°N, 23.7°E), Greece. Based on Köppen-Geiger climatic classification, this climate is classified as Csa, namely warm temperate, dry, and hot summer [51]. Hence, the climate is considered suitable for the cooling and ventilation purposes of our SC-RC ventilation. This building has a 6 m by 6 m plan and a 3 m floor-to-ceiling height, atop with a 3 m high 45° gabled roof. On the two inclined sides of the gable roof, an SC and an RC cavity with air channel heights of 20 cm each are placed in opposition to one another, i.e.,

SC facing south to the direction of the sun and RC cavity facing north. The SC and RC cavity have 30 cm wide vertical roof openings interfacing with the outdoor air at the top of their air channel and 30 cm wide horizontal ceiling openings interfacing with the room air at the bottom of the air channel. There was also another opening located on the wall, at 40 cm above the floor with a 30 cm gap.

Case studies were designed based on the arrangement of the working openings. The first case study resembles a conventional SC ventilation, where the roof SC used the wall opening (henceforth 'SC+wall-opening'), as shown in Figure 2 (a). In the second case study, the wall opening was closed, and the roof RC opening was opened (henceforth 'SC-RC' in Figure 2 (b)). For the third case study, the wall and RC openings were both opened, and the case study was named the 'SC-RC+wall-opening' as shown in Figure 2 (c).

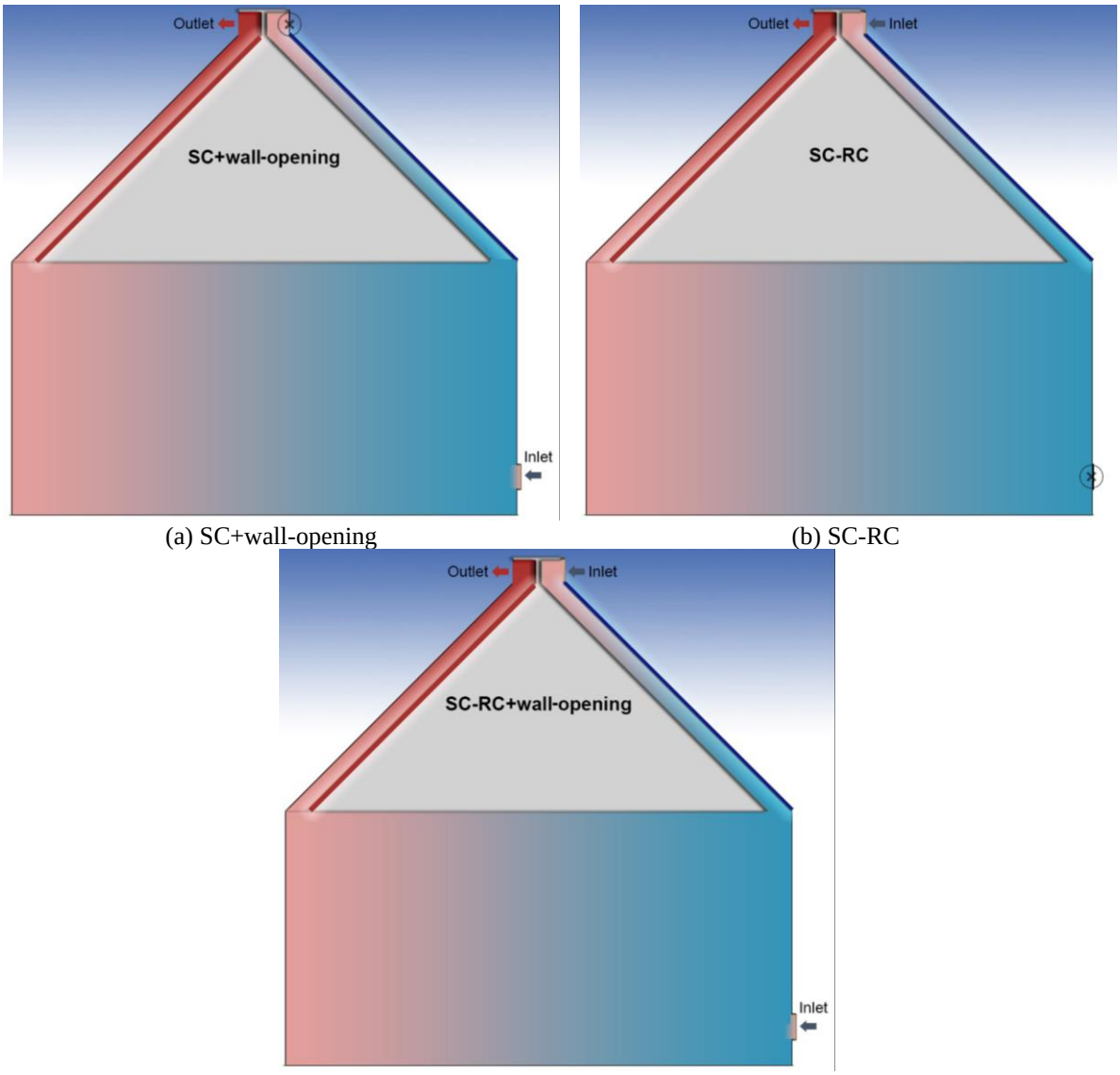

(a) SC+wall-opening (b) SC-RC

(c) SC-RC+wall-opening

Figure 2 Illustration of the case studies: (a) 'SC+wall-opening', (b) 'SC-RC', and (c) 'SC-RC+wall-opening'

Construction materials of the case study are based on the common construction materials for buildings in Athens, Greece. Brick was used for wall material with 20 cm of thickness, together with ceramic, timber, and roof tile for floor, ceiling, and roof materials, respectively [52]. Further, the absorber and emitter in the SC and RC cavity used 1 mm thick aluminium as its base, coated with hypothetical coating suited for its purpose. The absorber has high absorptivity/emissivity in the solar radiation band (0.2-3 μm) and thermal radiation band (3-25 μm). Whereas the emitter has high absorptivity/emissivity only in the atmospheric window band (8-13 μm) and low absorptivity/emissivity in solar (0.2-3 μm) and other thermal bands (3-8 μm; and 13-25 μm). Spectral properties of the construction materials in those wavelengths and their respective thermal properties are summarised in Table 1. Except for the absorber and emitter, the emissivity data for all materials were taken from the ECOSTRESS spectral library [53].

Table 1 Thermal and spectral properties of the construction materials

Material	**Thermal properties**			**Absorptivity/emissivity in the radiation band**			
	Thermal conductivity ($W \cdot m^{-1} \cdot K^{-1}$)	Density ($kg \cdot m^{-3}$)	Specific heat capacity ($J \cdot kg^{-1} \cdot K^{-1}$)	0.2-3 μm	3-8 μm	8-13 μm	13-25 μm
Brick	0.72	1920	840	0.79	0.77	0.93	0.93
Ceramic tile	0.8	1700	850	0.34	0.94	0.93	0.93
Insulation board	0.033	38	1400	0.70	0.90	0.90	0.90
Roof tile	0.8	1890	880	0.87	0.93	0.95	0.95
Timber	0.16	720	1260	0.46	0.9	0.94	0.94
Absorber	202.4	2719	871	0.95	0.95	0.95	0.95
Glass	1.38	2203	703	0.05	0.88	0.88	0.88
Emitter	202.4	2719	871	0.05	0.05	0.95	0.05

In addition to the description above, for the weather condition, we extracted the typical meteorological year (TMY) data of Athens from the EnergyPlus weather data website [54]. Specifically, we selected the average monthly data in the summer month of July, as it was the hottest period of the year in the location. Overview of weather conditions can be seen in Figure 3. Note that, to analyse the effect of the RC cavity in SC-RC ventilation, in this study, we only account for the buoyancy-driven ventilation flow generated by the SC and RC cavity. Therefore, the wind effect on ventilation is not considered yet in this study.

Besides comparing ventilation parameters of every case study relative to one another, the performance of the case studies was also compared with ventilation standards. We assumed the building to be a residential building and thus required to fulfil the ventilation requirement of a residential function. The requirements for ventilation rate and thermal comfort of a bedroom/living room building are 0.7 air changes per hour (ACH) based on ANSI/ASHRAE Standards [55]. Whereas for the cooling performance requirement, we analysed the thermal

comfort condition based on the adaptive thermal comfort model according to the ASHRAE Standard [56]. The adaptive thermal comfort model is appropriate to be used in a naturally ventilated building with the occupant's metabolic rate ranging from 1.0 to 1.3 met, roughly equal to near-sedentary physical activities. We used the room air temperature as the proxy for the operative temperature, which is considered adequate in the condition such as our case studies [56].

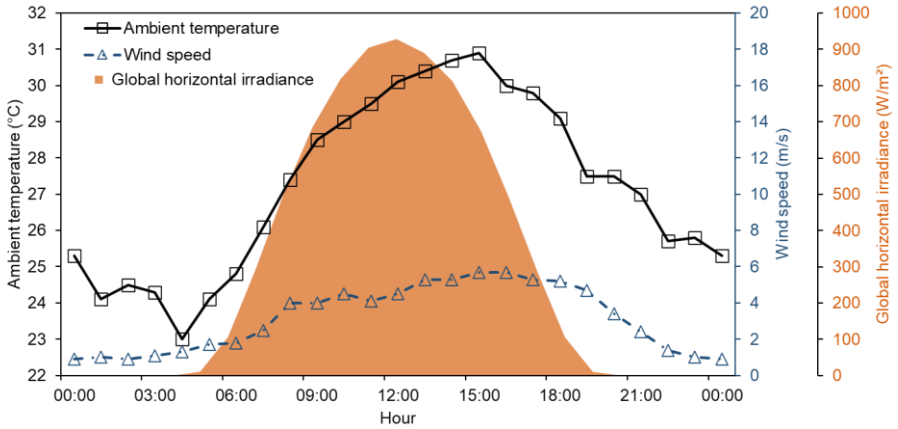

Figure 3 The average temperature, wind speed, and solar radiation during the summer month of July in Athens [54]

2.2. Buoyancy-driven flow in SC-RC ventilation

In principle, the flow direction through the building's openings in buoyancy-driven ventilation can be inferred by looking at the static pressure gradient inside and outside the building. The static pressure varies with height and density with the following relation, where P is the static (gauge) pressure, g is the gravitational acceleration, ρ is the density of the air, and z is the vertical distance (upward positive):

$$P = -g \int_0^z \rho \, dz \tag{1}$$

Generally, we can assume that the air density outside the building (ρ_0) is constant, yet the density of the indoor air (ρ) is a function of height, $\rho(z)$, due to thermal stratification. If we plot the difference between pressure outside and inside the building ($\Delta P = P_\mathrm{o} - P_\mathrm{i}$) along the vertical axis, for a warmer-than-ambient room, the pressure gradients would have the distribution as in Figure 4 (a) [57]. There is a level where the $\Delta P = 0$, and this level is called the neutral level. The condition where $\Delta P > 0$ below this neutral level indicating flow into the room, and $\Delta P < 0$ above this level indicating flow out of the room. When the room is colder than the ambient, the condition is reversed, i.e., $\Delta P < 0$ at the bottom indicating flow out of the room, and $\Delta P > 0$ at the top side of the room indicating inflow. See Figure 4 for the illustration of the ΔP relation to the flow direction.

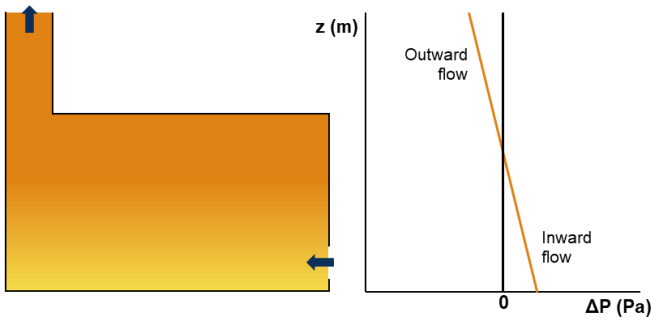

(a)

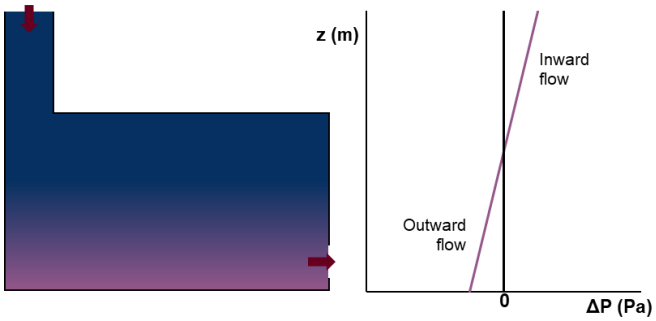

(b)

Figure 4 Flow direction and outdoor-indoor static pressure differences of (a) warm room and (b) cold room

In conventional SC ventilation, the warm indoor condition that drives the flow, as mentioned above, is provided by the solar radiation that is absorbed by the absorber in SC. While in an RC cavity, the opposite situation occurred; the cooling effect from the RC emitter could provide a potential downward flow in the RC cavity. Therefore, in the proposed SC-RC ventilation, the performance of SC is expected to be enhanced by the RC cavity as a buoyancy force assistant as well as a possible precooling air channel.

3. Methodology

3.1. Simulation steps

Performance evaluation of the SC-RC ventilation case studies was conducted using CFD simulation in ANSYS Fluent 2021 [58]. The simulation follows general steps, as shown by the diagram in Figure 5. After geometry creation, the model was then translated into a computational grid in the meshing step. Simulation and boundary condition settings could then be specified once the computational grid is completed. For this step, the solar irradiance and weather conditions were inputted. To represent a whole day simulation with a dynamic ambient condition, we converted the hourly data of solar irradiance and weather parameters into a tabular user-defined input for ANSYS Fluent 2021. Near the end of the simulation steps, simulation results were all checked for convergence as well as time step and grid independence study. This step is particularly important to make sure the results are not influenced by the time step or grid size. Parameters looked for the time step, and grid-

independence study were glass, absorber, and emitter surface temperature, room air temperature, and velocity, as well as the volumetric and mass flow rate at the building openings.

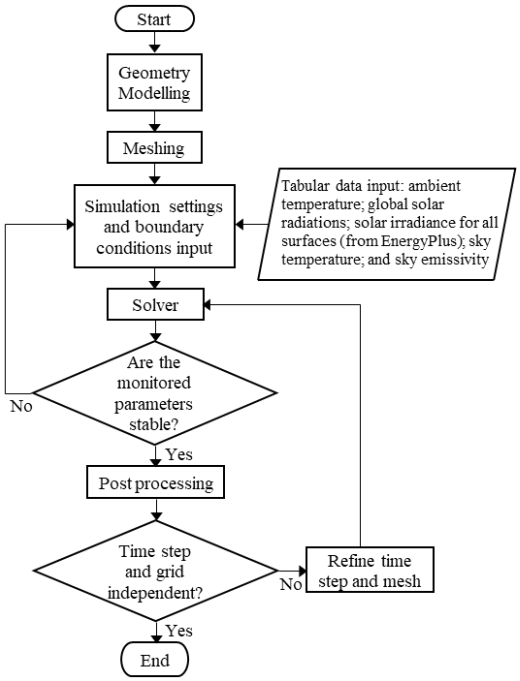

Figure 5 Simulation logic flow diagram

3.2. Geometry and meshing

The CFD simulation was done in 2D geometry, representing the cross-sectional model of the case studies. This is considered to be acceptable for an unchanging room shape [59]. And as the basic principles of buoyancy flow necessitate the condition of the outdoor pressure gradient in the vertical direction to be known, we include the exterior of the building in the geometrical model [59]. Figure 6 shows the geometry of the computational domain used in ANSYS Fluent. As described in Section 2, the building was 6 m wide (W) and 6 m high (H), including the room. Extension of the computational domain that represents the outdoor air was added by extending the boundary to 10 times its width (10W) and height (10H) in the respective directions. The top and side boundaries of the external domain were set as a pressure field far away, and the bottom boundary of the external domain was set as the ground, while the geometry of the building envelope was drawn based on case studies described in Section 2.1. There were three case studies simulated, and the difference between them was on the opening configurations. The mesh used for the simulation was hexahedral mesh started with a maximum mesh size of 5 cm for the room (Figure 7) and later refined for grid-independence study until the maximum size of 1 cm.

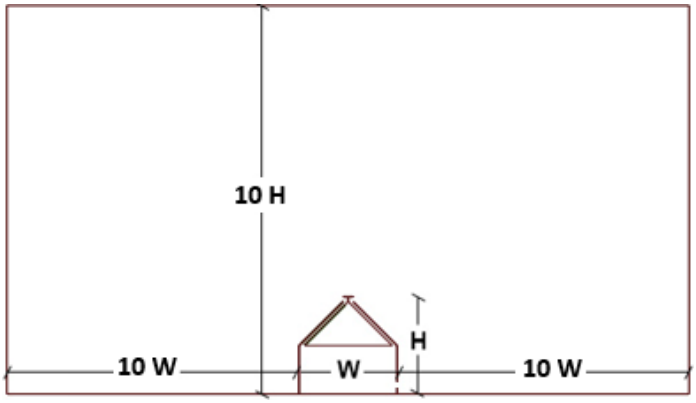

Figure 6 The computational domain of the study

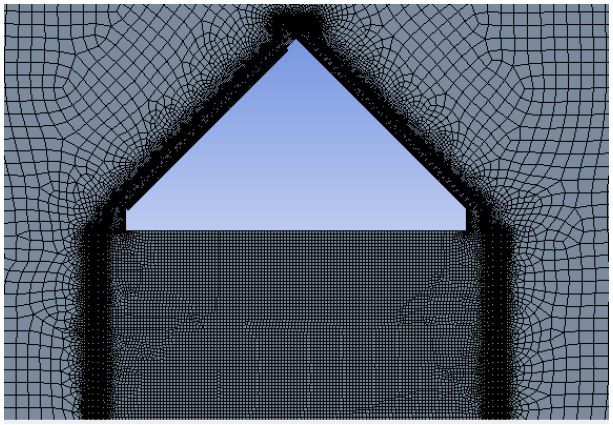
Figure 7 Initial computational grids with 5 cm maximum size in the room

3.3. Boundary conditions

To represent the heat transfer phenomena in the building we employed the user-defined functions (UDF) feature in ANSYS Fluent. Heat balance equations for surfaces of the building envelope as the basis of UDF are described in the following subsections.

3.3.1. Heat balance of the glass cover, RC emitter, roof, and external side of the wall

All the building's exterior surface exchanges heat via radiation with the sun (q_{sol}) and the sky (q_{rad}) as well as convection with the outdoor ambient air. At the interior side of the surface, another convection occurs between the glass and RC emitter to the adjacent air in the SC and RC cavity, and conduction heat transfer occurs on the roof and wall surfaces. Equation (2) formulates the heat balance. q_{sol} appears in the form of absorbed solar radiation and is detailed by Equation (3), where α_{surf} is the material's absorptivity, and H_{surf} is the total solar irradiation received by the surface. Moreover, q_{rad} has two components namely the sky radiation to the surface ($q_{\mathrm{rad\_sky}}$) and vice versa ($q_{\mathrm{rad\_surf}}$), and the two terms can be combined as shown in Equation (4), where $\varepsilon_{\mathrm{sky}}$ and $\varepsilon_{\mathrm{surf}}$ are emissivity of the sky and the surface respectively, σ is Stefan-Boltzmann constant, T_{sky} is the sky temperature, and T_{surf} is the surface temperature. To account for differences in the surface's inclination angle to the sky, we introduce the variable F_{surf} to Equation (4), which represents percentage of net RC power reduction

with the increase of inclination angle from 0° (horizontal surface) to 90° (vertical surface). Based on our experimental data, the value of F_{surf} for 45° (glass and emitter surfaces) and 90° (wall surfaces) are 0.75 and 0.33 respectively.

$$\begin{cases} q_{\text{sol}} + q_{\text{rad}} + h_{\text{amb}}(T_{\text{amb}} - T_{\text{surf}}) + h_{\text{channel}}(T_{\text{channel}} - T_{\text{surf}}) = 0, & \text{for glass and RC emitter} \\ q_{\text{sol}} + q_{\text{rad}} + h_{\text{amb}}(T_{\text{amb}} - T_{\text{surf}}) + q_{\text{cond}} = 0, & \text{for roof and wall} \end{cases} \quad (2)$$

$$q_{\text{sol}} = \alpha_{\text{surf}}\, H_{\text{surf}} \quad (3)$$

$$q_{\text{rad}} = q_{\text{rad\_sky}} - q_{\text{rad\_surf}} = F_{\text{surf}}\ \varepsilon_{\text{sky}}\, \varepsilon_{\text{surf}}\, \sigma\, ({T_{\text{sky}}}^4 - {T_{\text{surf}}}^4) \quad (4)$$

Furthermore, the $h_{\text{amb}}(T_{\text{amb}} - T_{\text{surf}})$ term in Equation (2) is the convective heat transfer between ambient air with the surfaces, where h_{amb} is the convective heat transfer coefficient, and T_{amb} and T_{surf} are the ambient and surface temperature. Convective heat transfer coefficient h_{amb} is calculated by empirical formula from Watmuff et al. [60] as shown in Equation 5, with v as the ambient wind speed.

$$h_{\text{amb}} = 2.8 + 3.0v \quad (5)$$

Another convection term, $h_{\text{channel}}(T_{\text{channel}} - T_{\text{surf}})$ represents the convective heat transfer between the glass and RC emitter with the air in the air channel (SC and RC cavity), with h_{channel} as the heat transfer coefficient, T_{channel} as the air temperature in the channel. Additionally, q_{cond} represents the conduction on the roof and wall. The abovementioned convection and conduction terms are calculated by ANSYS Fluent. In Equation (4), however, the value of sky emissivity ε_{sky} is calculated from an empirical formula by Jackson [61,62] while the sky temperature T_{sky} is calculated using an empirical formula from Swinbank [62,63] as displayed below in Equation (6) and Equation (7), with T_{amb} as the ambient temperature, taken from the EnergyPlus weather data website [54].

$$\varepsilon_{\text{sky}} = 1 - \left[0.261\, e^{-7.77\times10^{-4}(273.15-T_{\text{amb}}^2)}\right] \quad (6)$$

$$T_{\text{sky}} = 0.0552\, T_{\text{amb}}^{1.5} \quad (7)$$

3.3.2. Heat balance of the absorber and other interior surfaces

The absorber needs to be included in the UDF for boundary conditions because it also absorbs solar radiation as the external source in this model. Similar to Equation (2) for the roof, the heat balance of the absorber also consists of absorbed solar radiation, heat exchanges with the sky, convection, and conduction. Only, there are small changes in the detailed equations for those terms, as shown in Equation (8). For solar irradiation, the absorber only receive a portion of what is transmitted by the glass, and thus the q_{sol} term in Equation (2) is modified as $q_{\text{sol\_glass}}$ and detailed in Equation (9) with the introduction of $\tau_{\text{glass,sol}}$, which is solar transmissivity of the glass

which is around 88%. Likewise, the q_{rad} term in Equation (2) is modified as $q_{\mathrm{rad\_abs}}$ with the introduction of $\tau_{\mathrm{glass,atm}}$ or the glass transmissivity in the infrared band (around 5%) in Equation (10). Further, the change in convection terms is since the absorber exchanges heat with the SC air, not with the ambient air, thus the convective heat transfer appears as in Equation (8) with T_{abs} as the absorber temperature.

$$q_{\mathrm{sol\_glass}} + q_{\mathrm{rad\_abs}} + h_{\mathrm{channel}}(T_{\mathrm{channel}} - T_{\mathrm{abs}}) + q_{\mathrm{cond}} = 0 \tag{8}$$

$$q_{\mathrm{sol\_glass}} = \tau_{\mathrm{glass,sol}}\, \alpha_{\mathrm{abs}}\, H_{\mathrm{abs}} \tag{9}$$

$$q_{\mathrm{rad}} = \tau_{\mathrm{glass,atm}}\, F_{\mathrm{surf}}\, \varepsilon_{\mathrm{abs}}\, \varepsilon_{\mathrm{sky}}\, \sigma\, ({T_{\mathrm{sky}}}^4 - {T_{\mathrm{abs}}}^4) \tag{10}$$

Furthermore, all other interior surfaces of the building were set as coupled walls for conjugate heat transfer calculation in material interfaces [64]. Radiation heat transfer between surfaces was considered using the discrete ordinates (DO) radiation model. The emissivity of the walls, though, was set according to the materials. Details of the settings are provided in the Supplementary document.

3.3.3. Validation of the mathematical model for radiative cooling effect

To validate the mathematical model for the boundary condition, we used the experimental data from a double-covered photothermal and radiative cooling (PT-RC) module by Hu et al. [65]. The module was able to be a more efficient PT collector in daytime and RC emitter at nighttime compared to the conventional stand PT or RC system. Therefore, this module was chosen to validate the ANSYS Fluent simulation because the module utilised both solar absorber and RC emitter, which could represent our boundary condition model. The comparison between the simulation results with the experimental data is shown in Figure 8. In Figure 8 (a), the glass temperature in the PT-RC module resulted from the simulation agrees substantially with the experimental data, as is the case for the absorber temperature shown in Figure 8 (b). Quantitative assessment of the simulation results was done using the root mean square deviation (RMSD) as shown in Equation (11), with $X_{\mathrm{sim},i}$ is the simulation data point and $X_{\mathrm{exp},i}$ is the expeimental data point [65,66]. The RMSD value of the glass temperature and absorber temperature are 0.8% and 1.7 %, respectively.

$$RMSD = \sqrt{\frac{1}{n}\sum_{i=1}^{n}\left[\frac{(X_{\mathrm{sim},i} - X_{\mathrm{exp},i})}{X_{\mathrm{exp},i}}\right]^2} \tag{11}$$

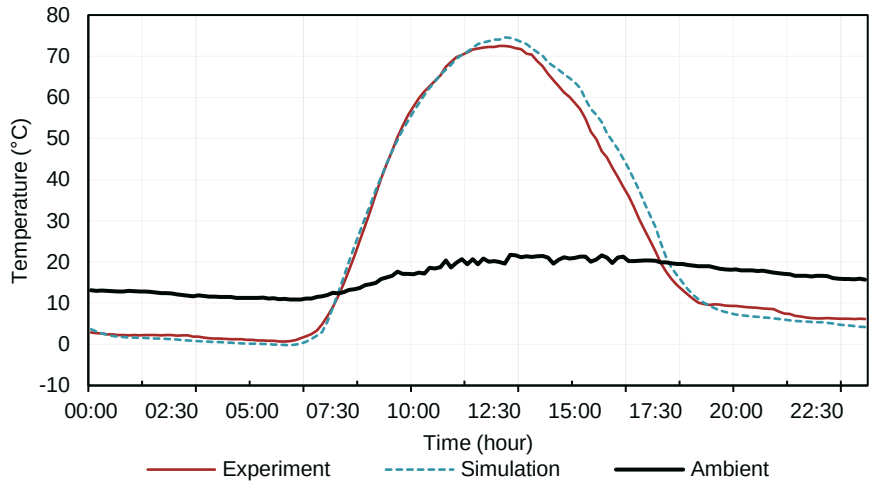

(a)

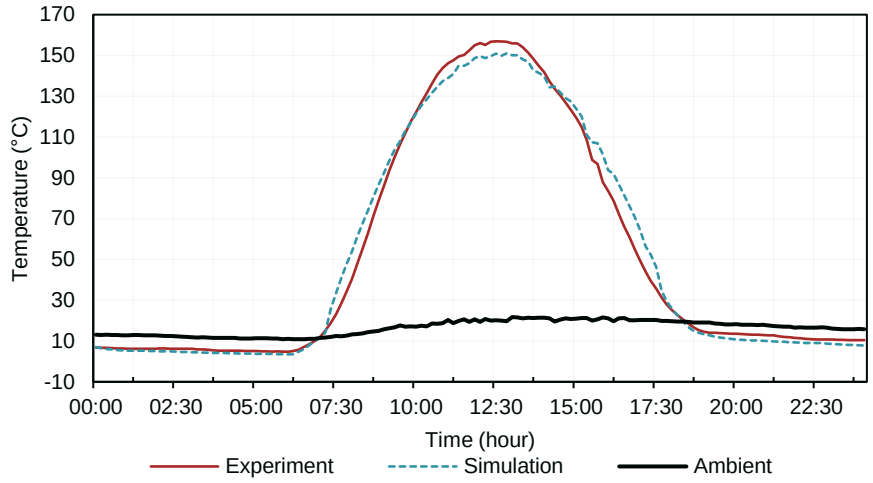

(b)

Figure 8 Comparison of experimental and simulation results of the PT-RC: (a) glass temperature and (b) absorber temperature

3.4. Solver settings

ANSYS Fluent 2021 was used to perform the CFD simulations [58]. The 2D transient Reynold-averaged Navier-Stokes equations were solved along with the Standard $k-\epsilon$ turbulence model [67], which is considered sufficient to model a buoyancy-driven ventilation flow [68,69]. The incompressible ideal gas law is used to handle the air, as the outdoor atmospheric pressure is set as constant [64]. For the radiation model, we used the DO radiation model due to its capability to account for the non-grey model and semi-transparent material (in this case, it is the glass cover in SC) [64]. The PISO algorithm was used for pressure velocity coupling. First-order discretisation scheme was used for both the convection and viscous terms of the governing equations, while the PRESTO! discretisation scheme was applied for the pressure terms. Simulations results were judged as converged when the key parameters, namely hourly indoor air temperature and velocity and flow rate at the building openings, show stable values.

3.5. Grid independence study

Grid and time independence studies were conducted to make sure the results were not dependent on the grid. Results from five combinations of grid and time-step sizes were analysed by comparing the important parameters used in the performance analysis, namely room air temperature, velocity, and volume flow rate. We checked the initial grid size (5 cm maximum) with 600 s time step size, and gradually reduced the grid size to 2.5 cm and 1 cm, and at 1 cm (finest grid size), decreased the time step to 450 s and 300. Figure 9 shows the comparison of three key parameters. From the 2.5 cm mesh size and 600 s time step, indoor air temperature and velocity results do not vary too much, with average relative variations between the mesh and time step sizes of 0.2°C for temperature and 0.02 m/s for velocity. However, the hourly pattern of the flow rate results only started to become closely matched with its subsequent grid and time step size at the 1 cm mesh size and 450 s time step size, with relative variations of 0.01 m³/s. Therefore, the grid and time step size used in this simulation is 1 cm and 450 s, respectively.

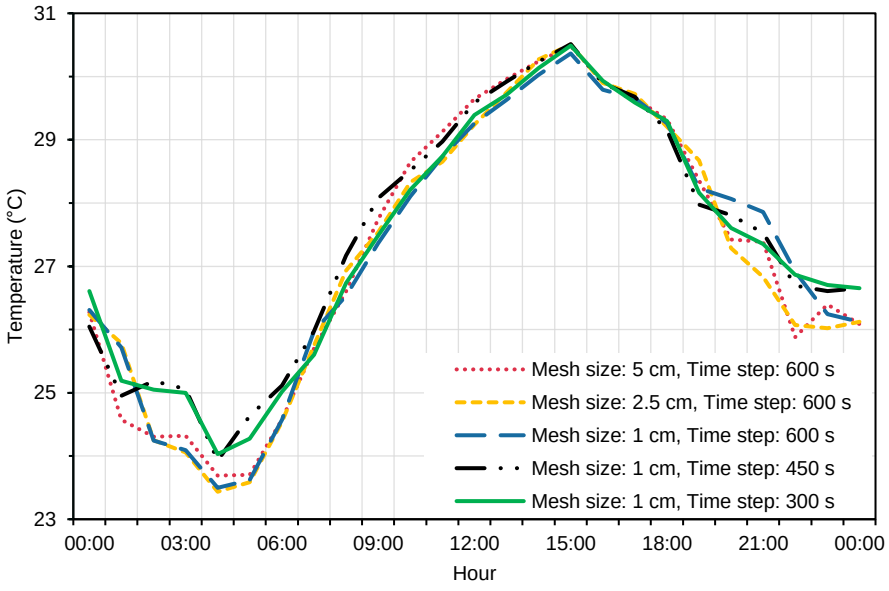

(a) Indoor air temperature

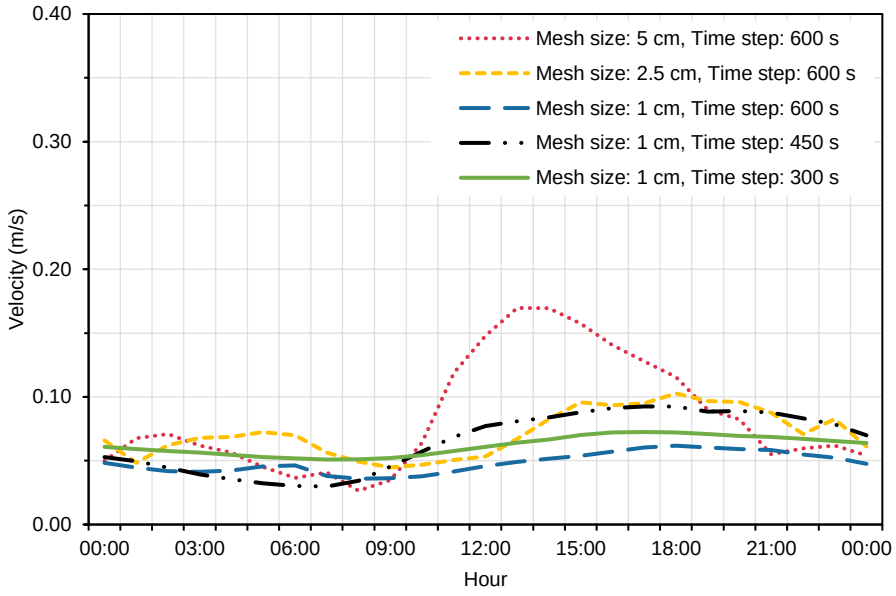

(b) Indoor air velocity

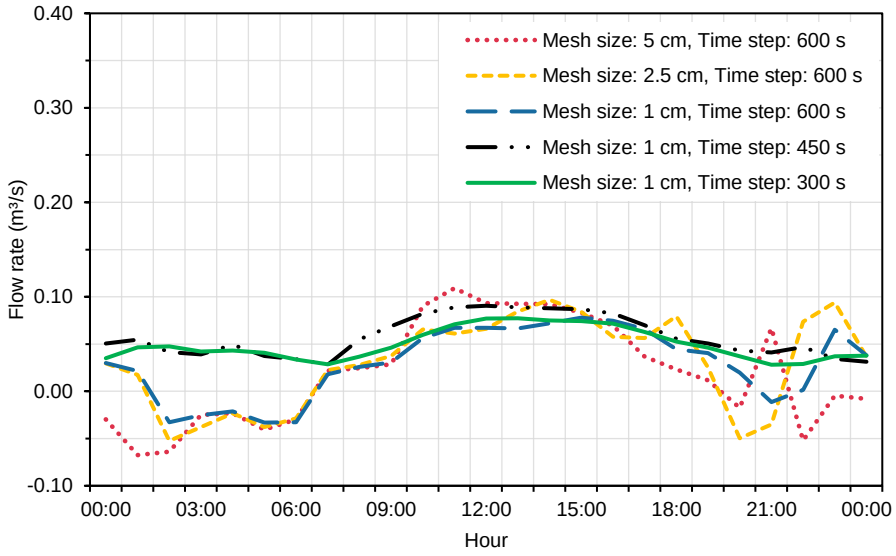

(c) Volume flow rate though the roof SC opening

Figure 9 Comparison of hourly pattern of the key parameters: (a) indoor air temperature, (b) indoor air velocity, and (c) volume flow rate through the SC opening; resulted from the different grid and time step sizes

3.6. Validation of solar chimney modelling

We validated the CFD simulation results with the experimental data of a solar chimney study by Chen et al. [70]. It was an experimental study incorporating a 1.5 m high chimney that was uniformly heated at one of the surfaces to represent solar absorption by the absorber wall. They tested the performance of the chimney in the different air gaps and different inclination angles, but the one that we used in this validation is the experimental setups with a similar air gap width and inclination angle with our study, which are 20 cm air channel width gap and 45° inclination angle. Detail of the experimental setup can be found in Chen et al. paper [70]. Four measured parameters from the experiment were compared with our simulation, i.e., vertical and horizontal temperature

profile, the horizontal velocity profile inside the chimney, as well as the airflow rate. Results for the temperature and velocity profiles are summarised in Figure 10. Overall, all the parameter profiles resulted from the simulation, including the flow rate (0.037 m^3/s compared to 0.035 m^3/s from the experiment), show close values with the experimental data. However, the model used for the near-wall treatment resulted in dissimilarities between the simulation and experiment in the horizontal temperature and velocity trends closed to the walls. Nonetheless, although the horizontal velocity profile between the simulation and experiment differed where it is closed to the walls, the airflow rate resulted from the simulations still shows a good agreement with the experiment, with RMSD values for temperature and velocity distributions inside the chimney of 3% and 14% respectively.

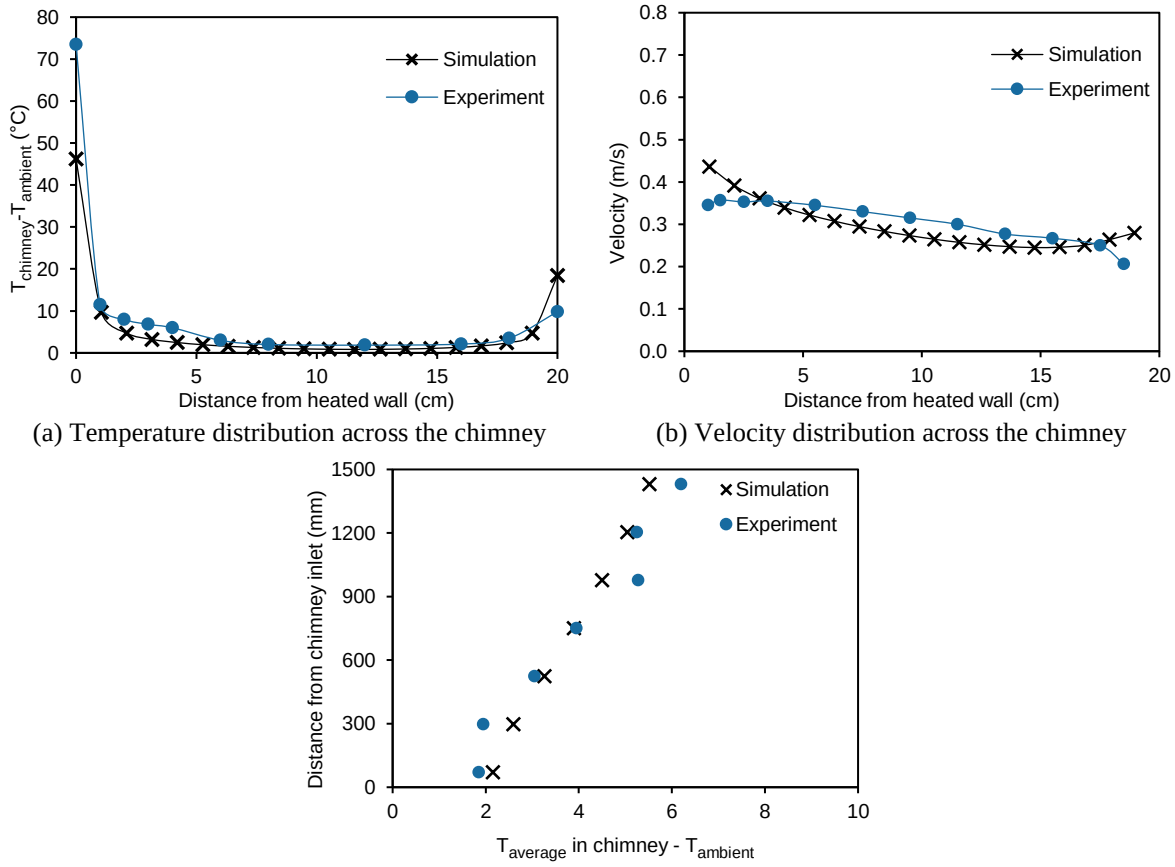

(a) Temperature distribution across the chimney

(b) Velocity distribution across the chimney

(c) Temperature distribution along the chimney

Figure 10 Comparison between the SC simulation and the experimental data [70]: (a) temperature and (b) velocity distribution across the solar chimney, and (c) temperature distribution along the solar chimney.

4. Results and Discussion

4.1. Effect of RC cavity on ventilation performance

Analysis of the flow rate through each opening (SC, RC, and wall openings) in the case studies hints at the effect of the RC cavity on the ventilation performance. Figure 11 (a) shows that the SC opening functions as an outlet, indicated by the negative flow rate, except in a few hours late at night. The outward flow in the SC opening peaks in the sunlit period and ambient temperature at its highest at 3 pm and gradually decreases until it reaches zero at

late night. In two case studies with wall openings, however, the decrease in outward flow rate continues until a reversed inward flow occurs at late night to early morning. Magnitude-wise, the flow rate through the SC opening is higher in the sunlit period than in the reversed flow period at night, with the highest and lowest daily average flow rate observed in 'SC-RC+wall-opening' and 'SC-RC', respectively.

Correspondingly, the hourly pattern of the flow direction through the wall opening represents the reversed direction of the SC opening flow but with some variations in the flow rate (Figure 11 (b)). On average, 'SC+wall-opening' has the highest inward flow rate through the wall opening during the daytime because all the ventilation flow enters through this opening only, while in the 'SC-RC+wall-opening' case, the inlet task is shared between two openings, namely the wall and RC openings. Figure 11 (b) shows that 'SC-RC+wall-opening' has a higher flow rate through the wall opening in the late-night (outward flow period). Also, Figure 11 (c) shows that the RC cavity flow rate in the 'SC-RC+wall-opening' case is even higher than the 'SC-RC' case during the late night until early morning. The enhancement of flow rate in the late-night to the morning period in the 'SC-RC+wall-opening' case coincides with the time of the optimal night sky cooling. This coincidence indicates the positive impact of RC emitter on the ventilation flow in the RC cavity when combined with the wall opening, as in the 'SC-RC+wall-opening' case.

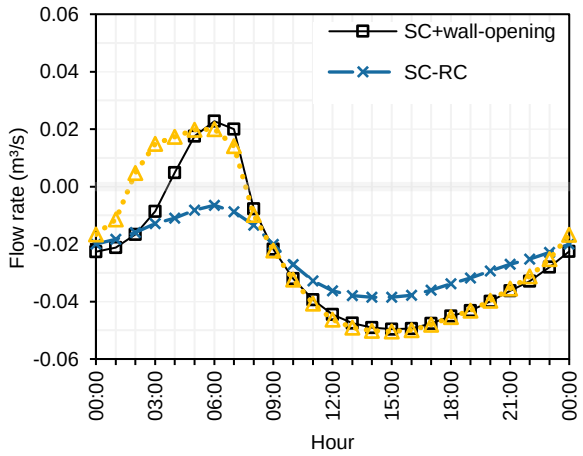

(a) Flow rate from the roof SC opening

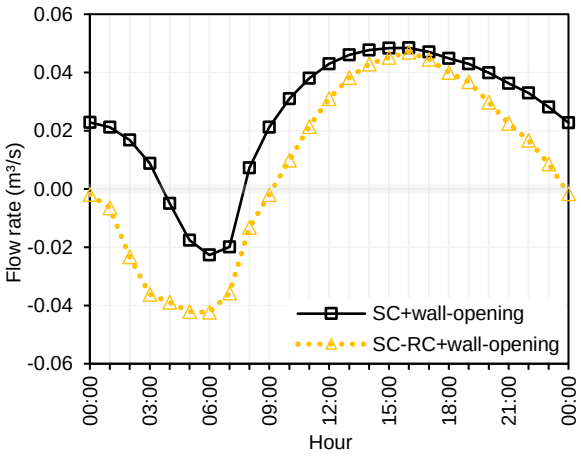

(b) Flow rate from the wall opening

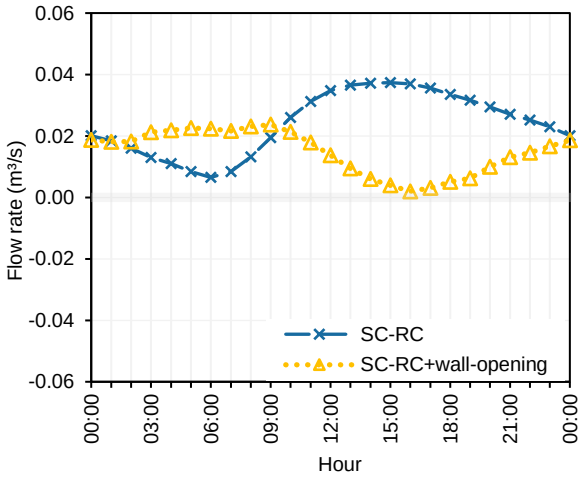

(c) Flow rate from the RC opening

Figure 11 Flow rate through the openings in each case study: (a) through the roof SC opening, (b) through the wall opening, (c) through the RC opening

To summarise the ventilation performance of the case studies from the abovementioned analysis, the outward flow rate data from all openings in each case study are combined and converted into ACH data, as shown in Figure 12. As a comparison, the line for the required minimum ACH (0.7 ACH) is also plotted. It is important to note that, unlike in the flow rate data where the negative value represents the outward flow and the positive value is the inward flow, the ACH value does not represent the flow direction, and its value is always positive. Therefore, in Figure 12, we see a pattern like a 'turning point' in the ACH graph, while in the flow rate data, it is the time when the reversed flow occurs. Moreover, from Figure 12, it is clear that the ventilation performance of all case studies starts to drop below the required minimum ACH around midnight. In all case studies, except 'SC-RC+wall-opening', the ventilation rate is reduced far below the 0.7 ACH standard, and even this sub-standard ACH period is prolonged until the morning. Unlike other case studies, the ACH of the 'SC-RC+wall-opening' case only falls slightly below the required minimum ACH, and it only occurs in a few hours. As indicated by Figure 12, the better performance from 'SC-RC+wall-opening' in the late night to early morning is the distinctive feature of this case study. Previous analysis on the flow rate of each opening hints at the RC cavity's role in providing more incoming air to the room during that period. Therefore, on average, 'SC-RC+wall-opening' has the best ventilation performance with 1.2 ACH compared to 1.0 ACH by 'SC+wall-opening' and 0.8 ACH by SC-RC.

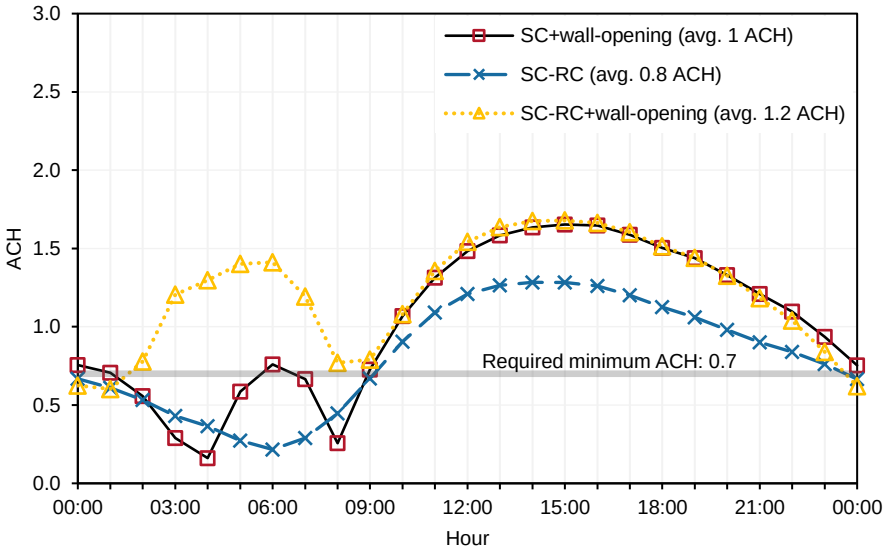

Figure 12 The hourly ACH of all case studies

4.2. Effect of RC cavity on passive cooling performance

Besides the ventilation performance, the effect of the RC cavity in providing cooling to the room is also evaluated. Figure 13 (a) shows the hourly indoor air temperature data from all case studies, alongside the ambient outdoor air temperature. As the ventilation rates of all case studies are closed to 1.0 ACH, the hourly profiles of indoor air temperature closely resemble the ambient outdoor air. During the daytime, the indoor air temperatures of all case studies are even slightly warmer than the ambient. Only, we can observe the sub-ambient room temperature in 'SC-RC' and 'SC-RC+wall-opening' at late night and early morning. Indeed, these cool indoor periods in the morning contribute to the daily average indoor air temperatures in 'SC-RC' (27.22°C) and 'SC-RC+wall-opening' (27.17 °C) being cooler than in 'SC+wall-opening' (27.45°C). Nonetheless, the average indoor air temperatures of all case studies are still within the 90% acceptability of thermal comfort limits (23-28°C) [71].

We can also separate the average indoor air temperature between daytime (6 am to 6 pm) and nighttime (6 pm to 6 am). As shown in Table 2, in the daytime, 'SC-RC' has the coolest room (28.79°C) with an average temperature similar to the ambient, while other case studies have their daytime average temperature higher than the ambient. The average daytime data suggests that the cooling power on the RC cavity cannot provide a sub-ambient room air temperature, although when compared to case studies without the RC cavity, it still performs better in managing the indoor air temperature. Consistent with the daytime performance, during the night, case studies with RC cavity are cooler, with 'SC-RC+wall-opening' has the coolest room (25.51°C) among all. The nighttime average temperatures from SC-RC and 'SC-RC+wall-opening' are sub-ambient and hence demonstrate the potential of the RC cavity to provide cool air during the night.

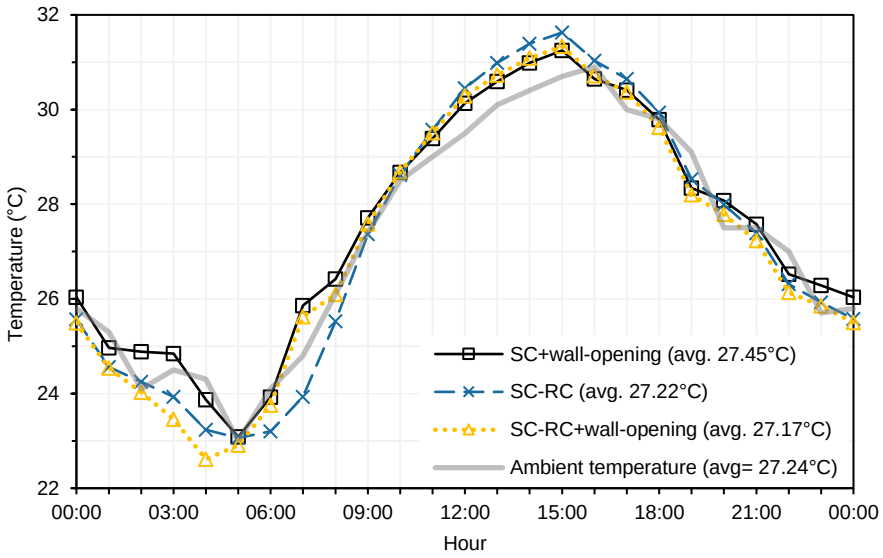

(a) Hourly indoor air temperature

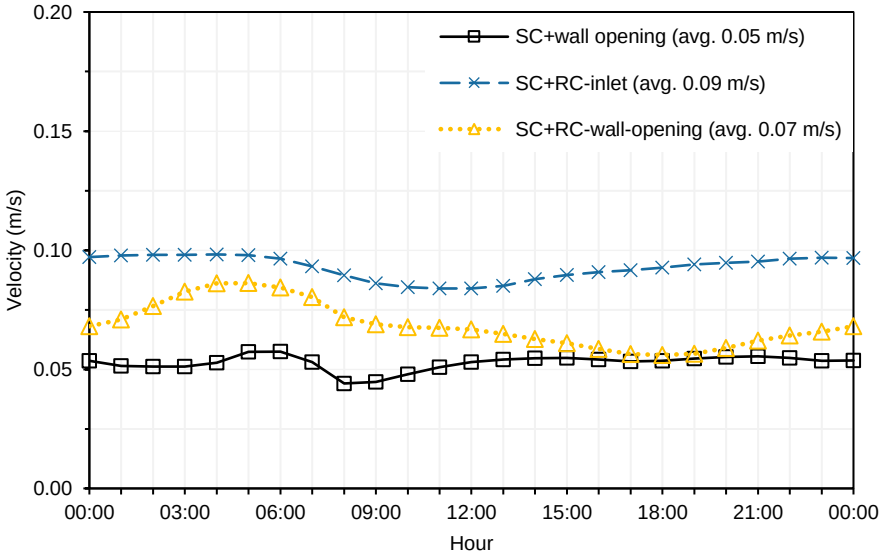

(b) Hourly indoor air velocity

Figure 13 The hourly (a) indoor air temperature and (b) indoor air velocity of all case studies

Table 2 Daily, daytime, and nighttime average room temperature

	Ambient temperature (°C)	**SC+wall-opening (°C)**	**SC-RC (°C)**	**SC-RC+wall-opening (°C)**
Daily	27.24	27.45	27.22	27.17
Daytime (6 am - 6 pm)	28.56	28.91	28.79	28.88
Nighttime (6 pm - 6 am)	25.96	26.02	25.68	25.51

To assess the contribution of the RC cavity in cooling, we further compare the inlet air temperature from the wall opening in 'SC+wall-opening' with the RC cavity in SC-RC. The comparison is made relative to the corresponding indoor air temperature, i.e., how much higher or lower the inlet temperature compared to the indoor air temperature ($\Delta T_{\text{inlet}} = T_{\text{inlet}} - T_{\text{indoor}}$). Note that the RC cavity air temperature is measured at the ceiling opening after the incoming air passes through the whole length of the RC cavity. ΔT_{inlet} helps to assess whether

the inlet air potentially makes the room warmer or cooler. Figure 14 reveals a remarkable cooling effect that the RC cavity provides as an inlet. The ΔT_{inlet} of 'SC+wall-opening' barely reaches -1°C even with the reversed flow from the SC opening at late night, whereas the ΔT_{inlet} of 'SC-RC' exceeds -3°C during the night. In the daytime, moreover, the 'SC+wall-opening' only adds warmer air to the room, while the 'SC-RC' delivers slightly cooler air to the room. Using a better RC emitter may even provide more chilled incoming air through the RC cavity during the daytime.

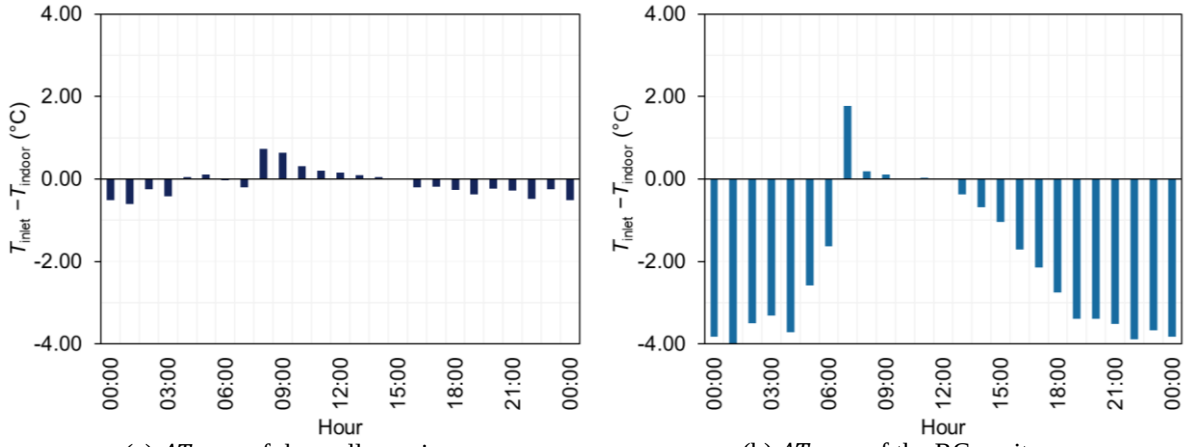

(a) ΔT_{inlet} of the wall opening (b) ΔT_{inlet} of the RC cavity

Figure 14 The ΔT_{inlet} comparison between the wall opening and RC cavity

Additionally, the cooling effect from the ventilation can also be provided by the breeze delivered into the room. To analyse the breeze delivered by each case study, we look at the hourly average velocity magnitude (Figure 13 (b)) and the velocity field in the room (Figure 15). As seen in Figure 13 (b), the indoor air velocities are below 0.1 m/s in all case studies, with the fastest breeze provided by 'SC-RC' (average 0.09 m/s). However, this value is considered too small to give a cooling sensation for the occupants because the breeze should be at least 0.3 m/s to create a sensation of cooling in a naturally ventilated building [56].

We can further analyse the effect of the RC cavity on the air velocity by looking at the velocity field and the corresponding temperature distribution of each case study at the warmest (3 pm) and cool (6 am) room air temperature. Comparing the 'SC+wall-opening' and 'SC-RC' cases in Figure 15, we can see how 'SC-RC' generates more breeze in the room due to its inlet position. Unlike the wall opening, the RC opening can push the incoming air deeper into the room and thus induce air movement in the room. However, because in the 'SC-RC+wall-opening' case, the inlet function is shared, and thus the flow rate from the RC cavity is reduced. Therefore the breeze delivered into the room by this case study is also slower than the SC-RC. Nonetheless, both case studies with RC cavity show the ability to create more breeze in the room than the conventional 'SC+wall-opening'.

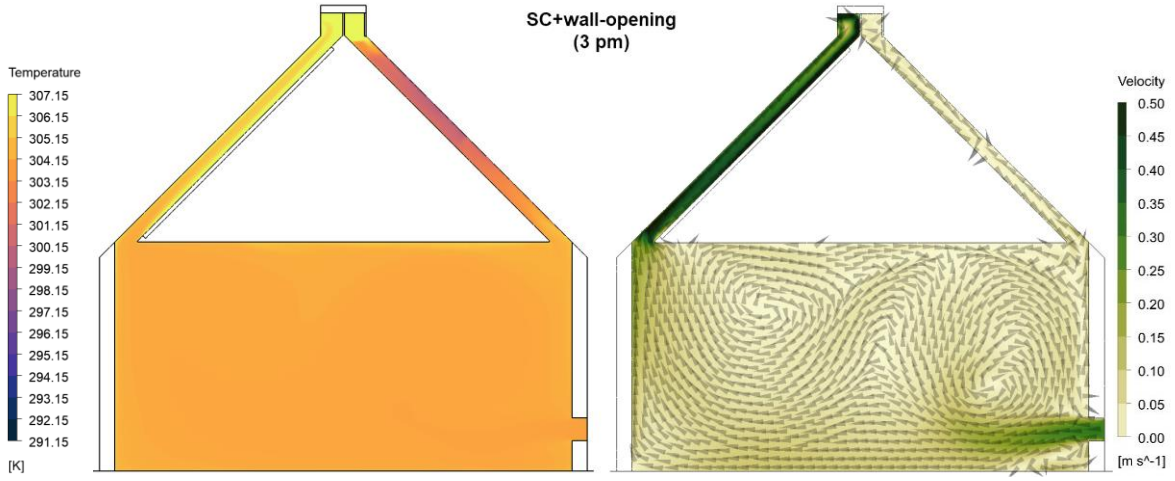
SC+wall-opening
(3 pm)
Temperature
307.15
306.15
305.15
304.15
303.15
302.15
301.15
300.15
299.15
298.15
297.15
296.15
295.15
294.15
293.15
292.15
291.15
[K]
Velocity
0.50
0.45
0.40
0.35
0.30
0.25
0.20
0.15
0.10
0.05
0.00
[m s^-1]

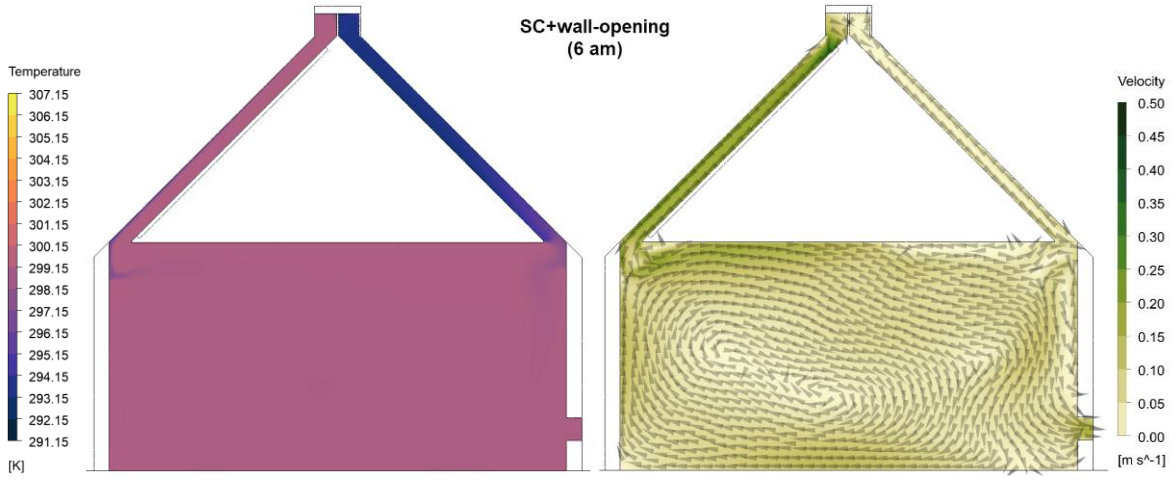
SC+wall-opening
(6 am)
Temperature
307.15
306.15
305.15
304.15
303.15
302.15
301.15
300.15
299.15
298.15
297.15
296.15
295.15
294.15
293.15
292.15
291.15
[K]
Velocity
0.50
0.45
0.40
0.35
0.30
0.25
0.20
0.15
0.10
0.05
0.00
[m s^-1]

(a)

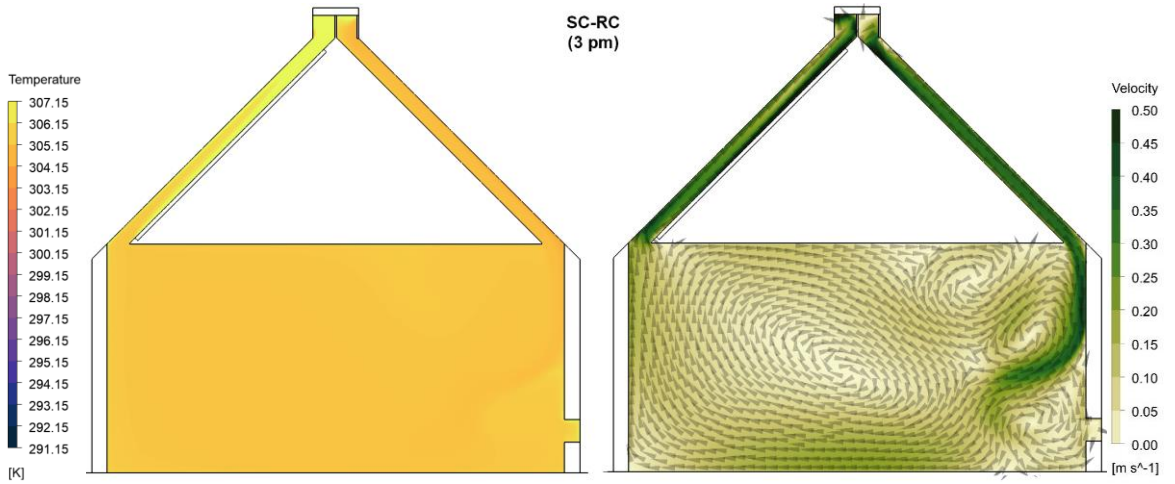
SC-RC
(3 pm)
Temperature
307.15
306.15
305.15
304.15
303.15
302.15
301.15
300.15
299.15
298.15
297.15
296.15
295.15
294.15
293.15
292.15
291.15
[K]
Velocity
0.50
0.45
0.40
0.35
0.30
0.25
0.20
0.15
0.10
0.05
0.00
[m s^-1]

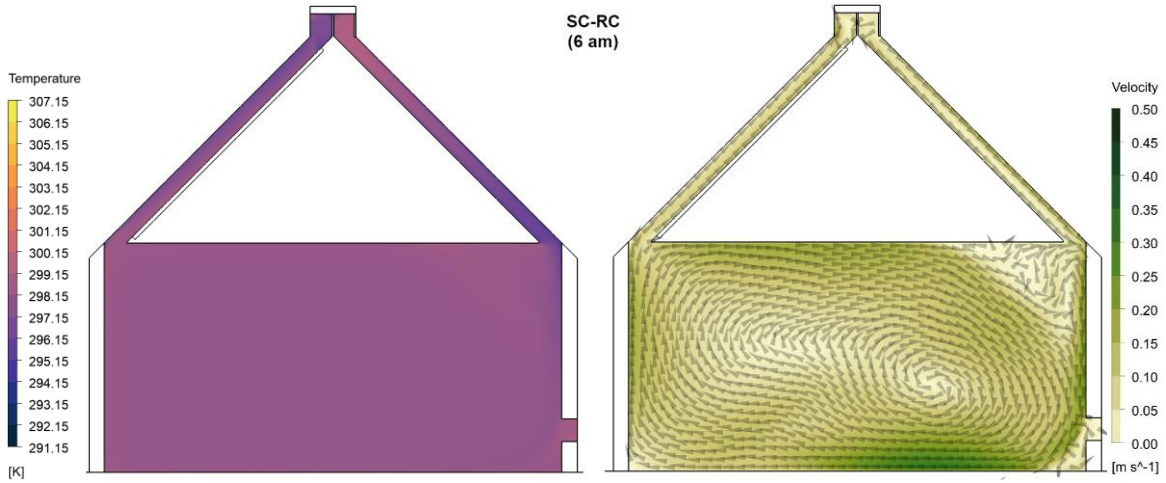

(b)

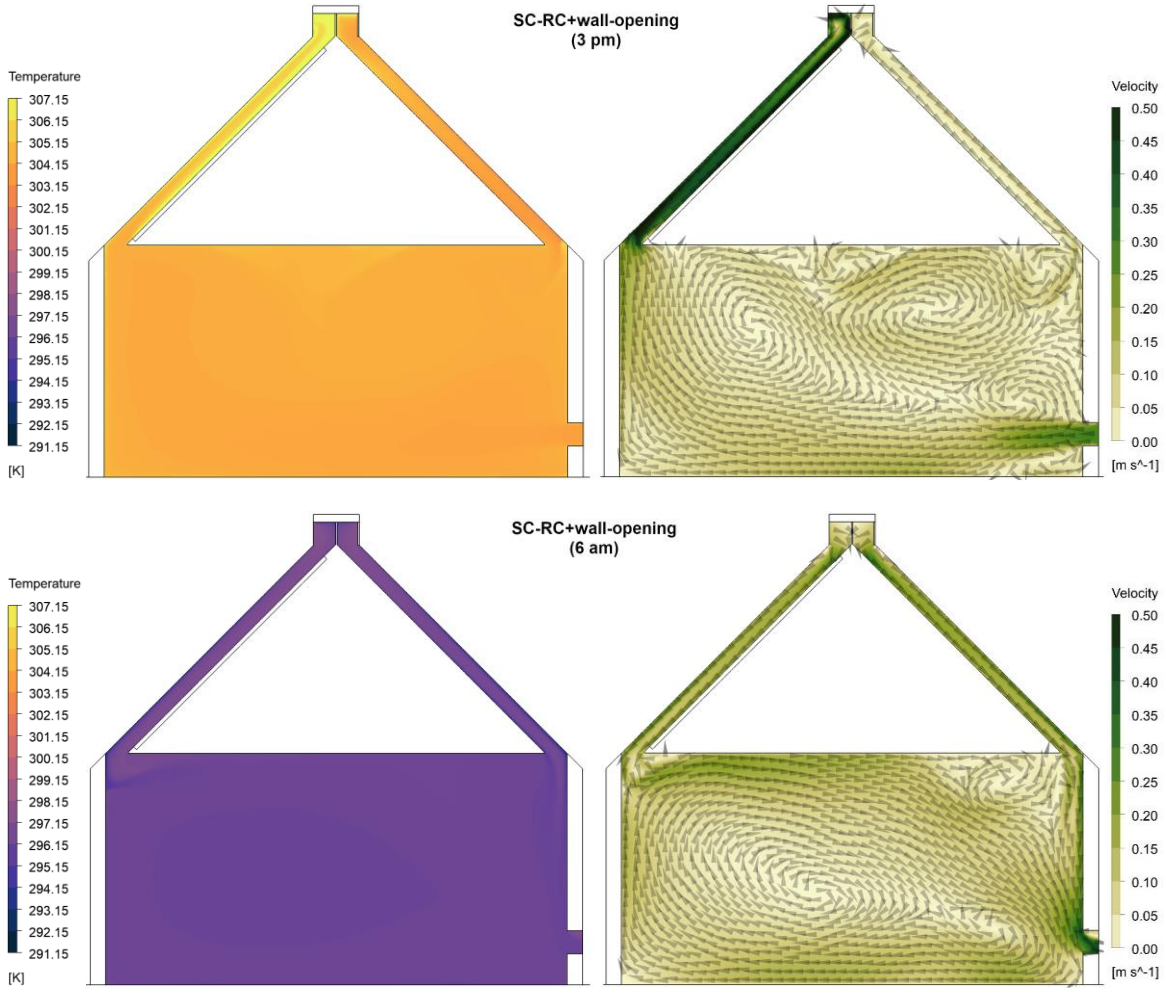

(c)

Figure 15 The temperature and velocity contour of the case studies at 3 pm and 6 am: (a) ‘SC+wall-opening’, (b) SC-RC, and (c) ‘SC-RC+wall-opening’

5. Conclusions

The performance of the combined solar chimney (SC) and radiative cooling (RC) ventilation has been evaluated. CFD simulations using ANSYS Fluent 2021 were conducted to assess three different configurations of SC-RC ventilation in the case study building. The case study building itself is a 6 m by 6 m room with a 3 m ceiling height, topped by a gabled roof with a tilt angle of 45°. Air channels were placed on both sides of the roof, one air channel on the sun-facing side as the SC and another on the other side as the RC cavity. Three different configurations of SC-RC ventilation were arranged based on the opening arrangement, namely the conventional roof SC with a wall opening ('SC+wall-opening'), the roof SC with an opening from the RC cavity ('SC-RC'), and the roof SC with both RC cavity and wall openings ('SC-RC+wall-opening'). A Mediterranean summer condition of Athens, Greece, was chosen as the climatic condition for the case studies.

In terms of ventilation performance, the 'SC-RC+wall-opening' case can preserve the ventilation performance even at late night until early morning when the other case studies even cannot achieve the required minimum ACH. The fact that this critical period intersects with the optimum night sky cooling period implies the role of the RC cavity in improving the 'SC-RC+wall-opening' ventilation performance. This is primarily indicated by the decline in the flow rate through both wall openings in the late night until early morning in the SC+wall-opening. The highest to the lowest ACH values for all case studies are 'SC-RC+wall-opening' with 1.2 ACH, 'SC+wall-opening' with 1 ACH, and 'SC-RC' with 0.8 ACH.

Moreover, the RC cavity can also potentially be a passive precooling channel for the incoming fresh air. It is observed from the daily average room air temperature that two cases with RC cavity (27.22°C for 'SC-RC' and 27.17°C for 'SC-RC+wall-opening') have cooler indoor air temperatures than the other cases without RC cavity (27.45°C for the 'SC+wall-opening'). The cooling effect of the RC cavity is more apparent when looking at the differences between the inlet air temperature with the room air temperature ΔT_{inlet} of the 'SC+wall-opening' and 'SC-RC' cases. Differing from the 'SC+wall-opening' that lets warmer air enters the room in the daytime, the inlet air temperature in the 'SC-RC' case always introduces cooler air into the room throughout the day. At night, the incoming air from the RC cavity is even more than 3°C lower than the room air temperature. There is, however, a substantial variation between daytime temperature (28.88°C daytime compared to 25.51°C nighttime average in 'SC-RC+wall-opening'), which could be overcome by using an RC emitter with higher daytime cooling power and adding an insulation material to the wall. In conclusion, this study shows that combining the RC cavity with the SC can enhance the ventilation and cooling performance of conventional SC ventilation.

Further, it should be noted that the present study only considers the latitude of the location. Also, the case studies did not put into consideration the internal heat gain and solar fenestration from windows. The exclusion of internal heat gain and window, together with the use of 2D CFD simulation and exclusion of the wind effect on the ventilation flow, are made to simplify the ventilation flow and focus the study only on the buoyancy-driven flow induced by the SC and RC cavity. Nevertheless, we recognise that in a real situation, when there is a considerable wind speed, some internal heat gains, and solar fenestration through windows, the indoor temperature and flow pattern might be significantly different than those considered in our study. Performance of this SC-RC ventilation in other latitudes and climate conditions as well as the effect of other determinant factors such as internal heat gain, solar fenestration, and ambient wind speed may be investigated in future studies.

6. Acknowledgments

This research was supported with a PhD studentship funded by Indonesia Endowment Fund for Education (Lembaga Pengelola Dana Pendidikan), Ministry of Finance, Republic of Indonesia, reference number S-2401/LPDP.4/2019 and H2020 Marie Skłodowska-Curie Actions-Individual Fellowships (842096).

7. References

1. Delmastro, C.; Dulac, J.; Abergel, T. Cooling Available online: http://iea.org (accessed on Dec 22, 2019).

2. Ahmad, M.I.; Jarimi, H.; Riffat, S. *Nocturnal Cooling Technology for Building Applications*; Springer: Singapore, 2019;

3. Argiriou, A. Radiative Cooling. In *Passive cooling of buildings*; Matheos Santamouris, D.A., Ed.; Earthscan: New York, 2013; pp. 424–454.

4. Mahdavinejad, M.; Javanrudi, K. Assessment of Ancient Fridges: A Sustainable Method to Storage Ice in Hot-Arid Climates. *Asian Cult. Hist.* **2012**, *4*, doi:10.5539/ach.v4n2p133.

5. Lu, X.; Xu, P.; Wang, H.; Yang, T.; Hou, J. Cooling potential and applications prospects of passive radiative cooling in buildings: The current state-of-the-art. *Renew. Sustain. Energy Rev.* 2016, *65*, 1079–1097.

6. Hossain, M.M.; Gu, M. Radiative cooling: Principles, progress, and potentials. *Adv. Sci.* **2016**, doi:10.1002/advs.201500360.

7. Bhamare, D.K.; Rathod, M.K.; Banerjee, J. Passive cooling techniques for building and their applicability

in different climatic zones—The state of art. *Energy Build.* 2019, *198*, 467–490.

8. Naghshine, B.B.; Saboonchi, A. Optimized thin film coatings for passive radiative cooling applications. *Opt. Commun.* **2018**, *410*, 416–423, doi:10.1016/j.optcom.2017.10.047.

9. Kim, H.; Lenert, A. Optical and thermal filtering nanoporous materials for sub-ambient radiative cooling. *J. Opt. (United Kingdom)* **2018**, *20*, doi:10.1088/2040-8986/aacaa1.

10. Zhang, J.; Yuan, J.; Liu, J.; Zhou, Z.; Sui, J.; Xing, J.; Zuo, J. Cover shields for sub-ambient radiative cooling: A literature review. *Renew. Sustain. Energy Rev.* **2021**, *143*, 110959, doi:10.1016/j.rser.2021.110959.

11. Heidarinejad, G.; Farmahini Farahani, M.; Delfani, S. Investigation of a hybrid system of nocturnal radiative cooling and direct evaporative cooling. *Build. Environ.* **2010**, *45*, 1521–1528, doi:10.1016/j.buildenv.2010.01.003.

12. Jeong, S.Y.; Tso, C.Y.; Zouagui, M.; Wong, Y.M.; Chao, C.Y.H. A numerical study of daytime passive radiative coolers for space cooling in buildings. *Build. Simul.* **2018**, *11*, 1011–1028, doi:10.1007/s12273-018-0474-4.

13. Bergman, T.L. Active daytime radiative cooling using spectrally selective surfaces for air conditioning and refrigeration systems. *Sol. Energy* **2018**, *174*, 16–23, doi:10.1016/j.solener.2018.08.070.

14. Zhang, K.; Zhao, D.; Yin, X.; Yang, R.; Tan, G. Energy saving and economic analysis of a new hybrid radiative cooling system for single-family houses in the USA. *Appl. Energy* **2018**, *224*, 371–381, doi:10.1016/j.apenergy.2018.04.115.

15. He, W.; Yu, C.; Yang, J.; Yu, B.; Hu, Z.; Shen, D.; Liu, X.; Qin, M.; Chen, H. Experimental study on the performance of a novel RC-PCM-wall. *Energy Build.* **2019**, *199*, 297–310, doi:10.1016/j.enbuild.2019.07.001.

16. Shen, D.; Yu, C.; Wang, W. Investigation on the thermal performance of the novel phase change materials wall with radiative cooling. *Appl. Therm. Eng.* **2020**, *176*, 115479, doi:10.1016/j.applthermaleng.2020.115479.

17. Zhou, Y.; Zheng, S.; Zhang, G. A review on cooling performance enhancement for phase change materials integrated systems—flexible design and smart control with machine learning applications. *Build. Environ.*

2020, *174*, 106786, doi:10.1016/j.buildenv.2020.106786.

18. Mihalakakou, G.; Ferrante, A.; Lewis, J.O. *The cooling potential of a metallic nocturnal radiator*; 1998; Vol. 28;.

19. Etzion, Y.; Erell, E. *Thermal Storage Mass in Radiative Cooling Systems**; 1991; Vol. 26;.

20. Sameti, M.; Kasaeian, A. Numerical simulation of combined solar passive heating and radiative cooling for a building. *Build. Simul.* **2015**, *8*, 239–253, doi:10.1007/s12273-015-0215-x.

21. Li, N.; Wang, J.; Liu, D.; Huang, X.; Xu, Z.; Zhang, C.; Zhang, Z.; Zhong, M. Selective spectral optical properties and structure of aluminum phosphate for daytime passive radiative cooling application. *Sol. Energy Mater. Sol. Cells* **2019**, *194*, 103–110, doi:10.1016/j.solmat.2019.01.036.

22. Hossain, M.M.; Jia, B.; Gu, M. A Metamaterial Emitter for Highly Efficient Radiative Cooling. *Adv. Opt. Mater.* **2015**, *3*, 1047–1051, doi:10.1002/adom.201500119.

23. Chungloo, S.; Limmeechokchai, B. Application of passive cooling systems in the hot and humid climate: The case study of solar chimney and wetted roof in Thailand. *Build. Environ.* **2007**, *42*, 3341–3351, doi:10.1016/j.buildenv.2006.08.030.

24. Chungloo, S.; Limmeechokchai, B. Utilization of cool ceiling with roof solar chimney in Thailand: The experimental and numerical analysis. *Renew. Energy* **2009**, *34*, 623–633, doi:10.1016/j.renene.2008.05.026.

25. DeBlois, J.; Bilec, M.; Schaefer, L. Simulating home cooling load reductions for a novel opaque roof solar chimney configuration. *Appl. Energy* **2013**, *112*, 142–151, doi:10.1016/j.apenergy.2013.05.084.

26. Mokheimer, E.M.A.; Shakeel, M.R.; Al-Sadah, J. A novel design of solar chimney for cooling load reduction and other applications in buildings. *Energy Build.* **2017**, *153*, 219–230, doi:10.1016/j.enbuild.2017.08.011.

27. Maerefat, M.; Haghighi, A.P. Passive cooling of buildings by using integrated earth to air heat exchanger and solar chimney. *Renew. Energy* **2010**, *35*, 2316–2324, doi:10.1016/j.renene.2010.03.003.

28. Imran, A.A.; Jalil, J.M.; Ahmed, S.T. Induced flow for ventilation and cooling by a solar chimney. *Renew. Energy* **2015**, *78*, 236–244, doi:10.1016/j.renene.2015.01.019.

29. Saleem, A.A.; Bady, M.; Ookawara, S.; Abdel-Rahman, A.K. Achieving standard natural ventilation rate of dwellings in a hot-arid climate using solar chimney. *Energy Build.* **2016**, *133*, 360–370, doi:10.1016/j.enbuild.2016.10.001.

30. Zha, X.; Zhang, J.; Qin, M. Experimental and Numerical Studies of Solar Chimney for Ventilation in Low Energy Buildings. In Proceedings of the Procedia Engineering; Elsevier Ltd, 2017; Vol. 205, pp. 1612–1619.

31. Wei, D.; Qirong, Y.; Jincui, Z. A study of the ventilation performance of a series of connected solar chimneys integrated with building. *Renew. Energy* **2011**, *36*, 265–271, doi:10.1016/j.renene.2010.06.030.

32. Lei, Y.; Zhang, Y.; Wang, F.; Wang, X. Enhancement of natural ventilation of a novel roof solar chimney with perforated absorber plate for building energy conservation. *Appl. Therm. Eng.* **2016**, *107*, 653–661, doi:10.1016/j.applthermaleng.2016.06.090.

33. Asadi, S.; Fakhari, M.; Fayaz, R.; Mahdaviparsa, A. The effect of solar chimney layout on ventilation rate in buildings. *Energy Build.* **2016**, *123*, 71–78, doi:10.1016/j.enbuild.2016.04.047.

34. Shi, L. Theoretical models for wall solar chimney under cooling and heating modes considering room configuration. *Energy* **2018**, 925–938, doi:10.1016/j.energy.2018.10.037.

35. Frutos Dordelly, J.C.; El Mankibi, M.; Roccamena, L.; Remion, G.; Arce Landa, J. Experimental analysis of a PCM integrated solar chimney under laboratory conditions. *Sol. Energy* **2019**, *188*, 1332–1348, doi:10.1016/j.solener.2019.06.065.

36. Omara, A.A.M.; Mohammed, H.A.; Al Rikabi, I.J.; Abuelnour, M.A.; Abuelnuor, A.A.A. Performance improvement of solar chimneys using phase change materials: A review. *Sol. Energy* **2021**, *228*, 68–88, doi:10.1016/j.solener.2021.09.037.

37. Cao, Y.; Sinaga, N.; Pourhedayat, S.; Dizaji, H.S. Innovative integration of solar chimney ventilator, solar panel and phase change material; under real transient weather condition of Hong Kong through different months. *Renew. Energy* **2021**, *174*, 865–878, doi:10.1016/j.renene.2021.04.146.

38. Rabani, M.; Kalantar, V.; Rabani, M. Passive cooling performance of a test room equipped with normal and new designed Trombe walls: A numerical approach. *Sustain. Energy Technol. Assessments* **2019**, *33*, 69–82, doi:10.1016/j.seta.2019.03.005.

39. Moosavi, L.; Zandi, M.; Bidi, M.; Behroozizade, E.; Kazemi, I. New design for solar chimney with integrated windcatcher for space cooling and ventilation. *Build. Environ.* **2020**, *181*, 106785, doi:10.1016/j.buildenv.2020.106785.

40. Serageldin, A.A.; Abdelrahman, A.K.; Ookawara, S. Parametric study and optimization of a solar chimney passive ventilation system coupled with an earth-to-air heat exchanger. *Sustain. Energy Technol. Assessments* **2018**, *30*, 263–278, doi:10.1016/j.seta.2018.10.010.

41. Taurines, K. Energy and thermal analysis of an innovative earth-to-air heat exchanger: Experimental investigations. *Energy Build.* **2019**, *187*, 1–15, doi:10.1016/j.enbuild.2019.01.037.

42. Long, T.; Zheng, D.; Li, W.; Li, Y.; Lu, J.; Xie, L.; Huang, S. Numerical investigation of the working mechanisms of solar chimney coupled with earth-to-air heat exchanger (SCEAHE). *Sol. Energy* **2021**, *230*, 109–121, doi:10.1016/j.solener.2021.10.029.

43. Rabani, M. Performance analysis of a passive cooling system equipped with a new designed solar chimney and a water spraying system in an underground channel. *Sustain. Energy Technol. Assessments* **2019**, *35*, 204–219, doi:10.1016/j.seta.2019.07.005.

44. Sun, T.; Huang, X.; Chen, Y.; Zhang, H. Experimental investigation of water spraying in an indirect evaporative cooler from nozzle type and spray strategy perspectives. *Energy Build.* **2020**, *214*, 109871, doi:10.1016/j.enbuild.2020.109871.

45. Dai, Y.J.; Sumathy, K.; Wang, R.Z.; Li, Y.G. Enhancement of natural ventilation in a solar house with a solar chimney and a solid adsorption cooling cavity. **2003**, *74*, 65–75.

46. Maerefat, M.; Haghighi, A.P. Natural cooling of stand-alone houses using solar chimney and evaporative cooling cavity. *Renew. Energy* **2010**, *35*, 2040–2052, doi:10.1016/j.renene.2010.02.005.

47. Sayed, A.; Abdallah, H.; Yoshino, H.; Goto, T.; Enteria, N.; Radwan, M.M.; Eid, M.A. Integration of evaporative cooling technique with solar chimney to improve indoor thermal environment in the New Assiut City , Egypt. **2013**, 1–15.

48. Mandal, J.; Fu, Y.; Overvig, A.C.; Jia, M.; Sun, K.; Shi, N.N.; Zhou, H.; Xiao, X.; Yu, N.; Yang, Y. Hierarchically porous polymer coatings for highly efficient passive daytime radiative cooling. *Science (80-.).* **2018**, *362*, 315–319, doi:10.1126/science.aat9513.

49. Zhang, J.; Yuan, J.; Liu, J.; Zhou, Z.; Sui, J.; Xing, J.; Zuo, J. Cover shields for sub-ambient radiative cooling: A literature review. *Renew. Sustain. Energy Rev.* **2021**, *143*, 110959, doi:10.1016/j.rser.2021.110959.

50. Vilà, R.; Martorell, I.; Medrano, M.; Castell, A. Adaptive covers for combined radiative cooling and solar heating. A review of existing technology and materials. *Sol. Energy Mater. Sol. Cells* **2021**, *230*, doi:10.1016/j.solmat.2021.111275.

51. Kottek, M.; Grieser, J.; Beck, C.; Rudolf, B.; Rubel, F. World map of the Köppen-Geiger climate classification updated. *Meteorol. Zeitschrift* **2006**, *15*, 259–263, doi:10.1127/0941-2948/2006/0130.

52. Oikonomou, A.; Bougiatioti, F. Architectural structure and environmental performance of the traditional buildings in Florina, NW Greece. *Build. Environ.* **2011**, *46*, 669–689, doi:10.1016/j.buildenv.2010.09.012.

53. Meerdink, S.K.; Hook, S.J.; Roberts, D.A.; Abbott, E.A. The ECOSTRESS spectral library version 1.0. *Remote Sens. Environ.* **2019**, *230*, 111196, doi:10.1016/j.rse.2019.05.015.

54. EnergyPlus Weather Data Available online: energyplus.net/weather.

55. ANSI/ASHRAE ANSI/ASHRAE Standard 62.1-2019 Ventilation for Acceptable Indoor Air Quality 2019.

56. ANSI/ASHRAE ANSI/ASHRAE Standard 55-2020 Thermal Environmental Conditions for Human Occupancy 2020.

57. Chenvidyakarn, T. *Buoyancy effects on natural ventilation*; Cambridge University Press, 2013; ISBN 1107015308.

58. Ansys® Ansys Fluent 2021 R1, Help System, Fluent User's Guide, Getting Started, ANSYS, Inc.

59. Cook, M.J. An evaluation of computational fluid dynamics for modelling buoyancy-driven displacement ventilation. **1998**.

60. Watmuff, J.; Charters, W.; Proctor, D. Solar and wind induced external coefficients - Solar collectors. *Coop. Mediterr. pour l'Energie Sol.* **1977**, *1*, 56.

61. Idso, S.B.; Jackson, R.D. Thermal radiation from the atmosphere. *J. Geophys. Res.* **1969**, *74*, 5397–5403.

62. Evangelisti, L.; Guattari, C.; Asdrubali, F. On the sky temperature models and their influence on buildings energy performance: A critical review. *Energy Build.* **2019**, *183*, 607–625, doi:10.1016/j.enbuild.2018.11.037.

63. Swinbank, W.C. Long-wave radiation from clear skies. *Q. J. R. Meteorol. Soc.* **1963**, *89*, 339–348, doi:10.1002/qj.49708938105.

64. Ansys® Ansys Fluent 2021 R1, Help System, Fluent User's Guide, Solution Mode, ANSYS, Inc.

65. Hu, M.; Zhao, B.; Ao, X.; Chen, N.; Cao, J.; Wang, Q.; Su, Y.; Pei, G. Feasibility research on a double-covered hybrid photothermal and radiative sky cooling module. *Sol. Energy* **2020**, *197*, 332–343, doi:10.1016/j.solener.2020.01.022.

66. Bahaidarah, H.; Subhan, A.; Gandhidasan, P.; Rehman, S. Performance evaluation of a PV (photovoltaic) module by back surface water cooling for hot climatic conditions. *Energy* **2013**, *59*, 445–453, doi:10.1016/j.energy.2013.07.050.

67. Launder, B.E.; Spalding, D.B. *Lectures in Mathematical Models of Turbulence*; Academic Press: London, England, 1972;

68. Gan, G. Impact of computational domain on the prediction of buoyancy-driven ventilation cooling. *Build. Environ.* **2010**, *45*, 1173–1183, doi:10.1016/j.buildenv.2009.10.023.

69. Gilani, S.; Montazeri, H.; Blocken, B. CFD simulation of stratified indoor environment in displacement ventilation: Validation and sensitivity analysis. *Build. Environ.* **2016**, *95*, 299–313, doi:10.1016/j.buildenv.2015.09.010.

70. Chen, Z.D.; Bandopadhayay, P.; Halldorsson, J.; Byrjalsen, C.; Heiselberg, P.; Li, Y. An experimental investigation of a solar chimney model with uniform wall heat flux. *Build. Environ.* **2003**, *38*, 893–906, doi:10.1016/S0360-1323(03)00057-X.

71. Tartarini, F.; Schiavon, S.; Cheung, T.; Hoyt, T. CBE Thermal Comfort Tool: Online tool for thermal comfort calculations and visualizations. *SoftwareX* **2020**, *12*, 100563, doi:10.1016/j.softx.2020.100563.